

## RESEARCH ARTICLE

# Regulating *f* orbital of Tb electronic reservoir to activate stepwise and dual-directional sulfur conversion reaction

Shuang Yu<sup>1</sup> | Shuo Yang<sup>1,2</sup>  | Dong Cai<sup>1</sup>  | Huagui Nie<sup>1</sup> | Xuemei Zhou<sup>1</sup> | Tingting Li<sup>1</sup> | Ce Liang<sup>1</sup> | Haohao Wang<sup>2</sup> | Yangyang Dong<sup>1</sup> | Rui Xu<sup>1</sup> | Guoyong Fang<sup>1</sup> | Jinjie Qian<sup>1</sup> | Yongjie Ge<sup>1</sup> | Yue Hu<sup>1</sup> | Zhi Yang<sup>1</sup> 

<sup>1</sup>Key Laboratory of Carbon Materials of Zhejiang Province, Wenzhou University, Wenzhou, China

<sup>2</sup>College of Electrical and Electronic Engineering, Wenzhou University, Wenzhou, China

## Correspondence

Shuo Yang, Dong Cai, and Zhi Yang, Key Laboratory of Carbon Materials of Zhejiang Province, Wenzhou University, Wenzhou, 325035, China.

Email: yangshuo@wzu.edu.cn, caidong@wzu.edu.cn, and yang201079@126.com

## Funding information

Major Scientific and Technological Innovation Project of Wenzhou City, Grant/Award Number: ZG2021013; National Natural Science Foundation of China, Grant/Award Numbers: 22109119, 51972238, U21A2081; Natural Science Foundation of Zhejiang Province, Grant/Award Numbers: LQ19B030006, LQ22B030003; Postgraduate Innovation Foundation of Wenzhou University, Grant/Award Number: 316202102051

## Abstract

The sluggish kinetics in multistep sulfur redox reaction with different energy requirements for each step, is considered as the crucial handicap of lithium–sulfur (Li–S) batteries. Designing an electron reservoir, which can dynamically release electron to/accept electron from sulfur species during discharge/charge, is the ideal strategy for realizing stepwise and dual-directional polysulfide electrocatalysis. Herein, a single Tb<sup>3+/4+</sup> oxide with moderate unfilled *f* orbital is synthesized as an electron reservoir to optimize polysulfide adsorption via Tb–S and N··Li bonds, reduce activation energy barrier, expedite electron/Li<sup>+</sup> transport, and selectively catalyze both long-chain and short-chain polysulfide conversions during charge and discharge. As a result, Tb electron reservoir enables stable operation of low-capacity decay (0.087% over 500 cycles at 1 C), high sulfur loading (5.2 mg cm<sup>-2</sup>) and electrolyte-starved (7.5 μL mg<sup>-1</sup>) Li–S batteries. This work could unlock the potential of *f* orbital engineering for high-energy battery systems.

## KEYWORDS

electronic reservoir, lithium–sulfur battery, sulfur redox reaction kinetics, unfilled *f* orbital

## 1 | INTRODUCTION

Ever-increasing requirements for better electric vehicles and mobile electronics have motivate researchers to develop advanced energy storage systems with higher energy and power density than the current Li-ion batteries.<sup>1,2</sup> Among potential candidates, lithium–sulfur (Li–S) battery holds great promise for next-generation energy storage applications owing to a high theoretical capacity of sulfur at

1672 mAh g<sup>-1</sup>, which provides an ultrahigh energy density of 2600 Wh kg<sup>-1</sup>.<sup>3–5</sup> Unfortunately, Li–S batteries are plagued with the complex multielectron and multiphase sulfur redox reaction (SRR) that normally induces sluggish charge transfer kinetics and the accumulation and shuttling of soluble lithium polysulfides (LiPSs) within a working cell, which must be addressed for their commercialization.<sup>6</sup>

The commonly reported strategies based on physical confinement<sup>7</sup> and chemical adsorption<sup>8</sup> are insufficient

This is an open access article under the terms of the [Creative Commons Attribution](https://creativecommons.org/licenses/by/4.0/) License, which permits use, distribution and reproduction in any medium, provided the original work is properly cited.

© 2022 The Authors. *InfoMat* published by UESTC and John Wiley & Sons Australia, Ltd.

to solve these issues owing to their poor affinity to LiPSs and inferior ability to accelerate the LiPS conversion. Introducing electrocatalysts to accelerate the conversion kinetics of LiPSs and reduce the presence and migration of LiPSs in the electrolyte, has recently validated to overcome the above bottlenecks. However, from the fundamental point of view, the whole discharge and charge processes of Li-S batteries are accompanied by the stepwise sulfur electrochemical reactions, that is, Step I (discharge): a solid sulfur ( $S_8$ )-to-liquid LiPS conversion with a low energy barrier; Step II (discharge): a liquid LiPS-to-solid  $Li_2S_2/Li_2S$  conversion with a comparatively high energy barrier; Step III (charge): solid  $Li_2S_2/Li_2S$  undergoes a one-electron oxidation to form LiPS intermediates with a high energy barrier; and Step IV (charge): further oxidation of soluble LiPSs eventually yields  $S_8$  with a relatively low energy barrier, during which electrons are transferred to (discharge) or extracted from (charge) the sulfur species.<sup>9–13</sup> Obviously, the requirements toward electron and energy at each step of the consecutive SRR catalysis are different, a traditional single catalyst with simple ability of electronic gain or loss may not be able to accelerate all the steps in SRR to the maximum extent. Despite the extensive efforts on the simple combination of diverse catalytic materials (e.g., constructing heterojunction) to overcome their individual shortcomings for stepwise SRR, the poor interface joining and charge transfer between two or more compounds limit our ability to improve the electrode reaction kinetics.<sup>14,15</sup> Thus, designing an electron reservoir with a single catalyst material, which can dynamically release electrons to sulfur species (serve as an electron source) during discharging, while can rapidly accept electrons from sulfur species (serve as an electron drain) during charging, to activate both easy and difficult reaction steps and reduce the activation energy of the reactions is the ideal solution of smooth and consecutive SRR catalysis in discharging/charging Li-S batteries.

Rare earth elements are regarded as the promising candidates for electron reservoirs (source and drain) owing to their partially unfilled  $f$  electronic configurations.<sup>16</sup> Rare earth oxides are indispensable for synchronously catalyzing some complex and multielectron reaction systems, such as automobile exhaust gas purification (including HC/CO oxidation and NO reduction reactions<sup>17–19</sup>), due to their abundant electronic structures and flexible oxidation states and coordination numbers.<sup>20,21</sup> Among 17 rare earth elements, only terbium (Tb) has the characteristics of abundant valence states, the strong oxidizability, and non-radioactivity.<sup>22</sup> Typically, Tb with 8 electrons in  $4f$  shell adopts +3 oxidation state in oxides (Tb(III) oxide is defined as  $Tb^{3+}$  for short), which can be an electronic source and easily provides electrons to external species (Figure 1A). Tb with an oxidation state of +4 (Tb(IV) oxide is defined as  $Tb^{4+}$

for short) contains a half-filled  $4f$  shell,<sup>23</sup> which is like an electronic drain, endowing Tb with more possibilities of electron gain (Figure 1A). Thus,  $Tb^{4+}$  processes the high oxidizing power and high redox potential of 3.3 V versus NHE,<sup>24</sup> which can be a potential oxidant for sulfur oxidation reaction during charge. Inspired by the advantages from both  $Tb^{3+}$  and  $Tb^{4+}$ , we believe that it is desirable to develop a novel electron reservoir with spontaneous electron loss and capture capacity for a smooth SRR by utilizing the  $Tb^{3+}/Tb^{4+}$  couple.

In this work, a  $Tb^{3+/4+}$  electron reservoir supported on a N-doped graphene (Gh) conductive substrate (denoted as Gh- $Tb^{3+/4+}$ ) was prepared as cathode interlayer to activate a consecutive SRR in Li-S chemistry. Through systematically studying the SRR kinetics, activation energies, and reaction mechanisms by theoretical calculations, in situ spectroscopies, and electrochemical technologies, it is found that  $Tb^{3+}$  has good catalytic effect on long-chain LiPS conversion reactions (LCR, Step I and Step IV);  $Tb^{4+}$  is more inclined to accelerate short-chain LiPS conversion reactions (SCR, Step II and Step III);  $Tb^{3+/4+}$  with the proper unfilled  $f$  orbital electronic configurations and the merits of both  $Tb^{3+}$  and  $Tb^{4+}$ , can not only moderate the chemical affinity to LiPSs via bonding effect and provide fast electronic/ionic transportation but also can catalyze both LCR and SCR in tandem during charge/discharge processes (as shown in Figure 1A). As a result, Gh- $Tb^{3+/4+}$ -modified sulfur cathode exhibits a good battery performance even with a low catalyst loading, a high sulfur loading, and a low electrolyte/sulfur (E/S) ratio. Unfilled  $f$  orbital regulation and ever-changing valence states may offer valuable insights into developing highly active rare earth catalysts for high-performance Li-S batteries.

## 2 | RESULTS AND DISCUSSIONS

### 2.1 | Designing Tb electronic reservoir to facilitate SRR for Li-S batteries

It is well known that intrinsic electronic structures of catalyst materials determine their binding strength toward LiPSs and the energy barrier to sulfur conversion reactions.<sup>25</sup> Therefore, to predict the fundamental potential of Tb oxides with different valences in adsorbing and catalyzing LiPSs, the electronic structures of Tb oxides were firstly calculated by density functional theory (DFT). Considering the inactive aggregation of the Tb oxide catalyst during SRR process and the conductivity problem of catalyst system, N-doped Gh (labeled as Gh in this article if no special instructions) was introduced into the model constructions of catalysts (Figure S1) to anchor the catalyst well and improve the electron transmission of the

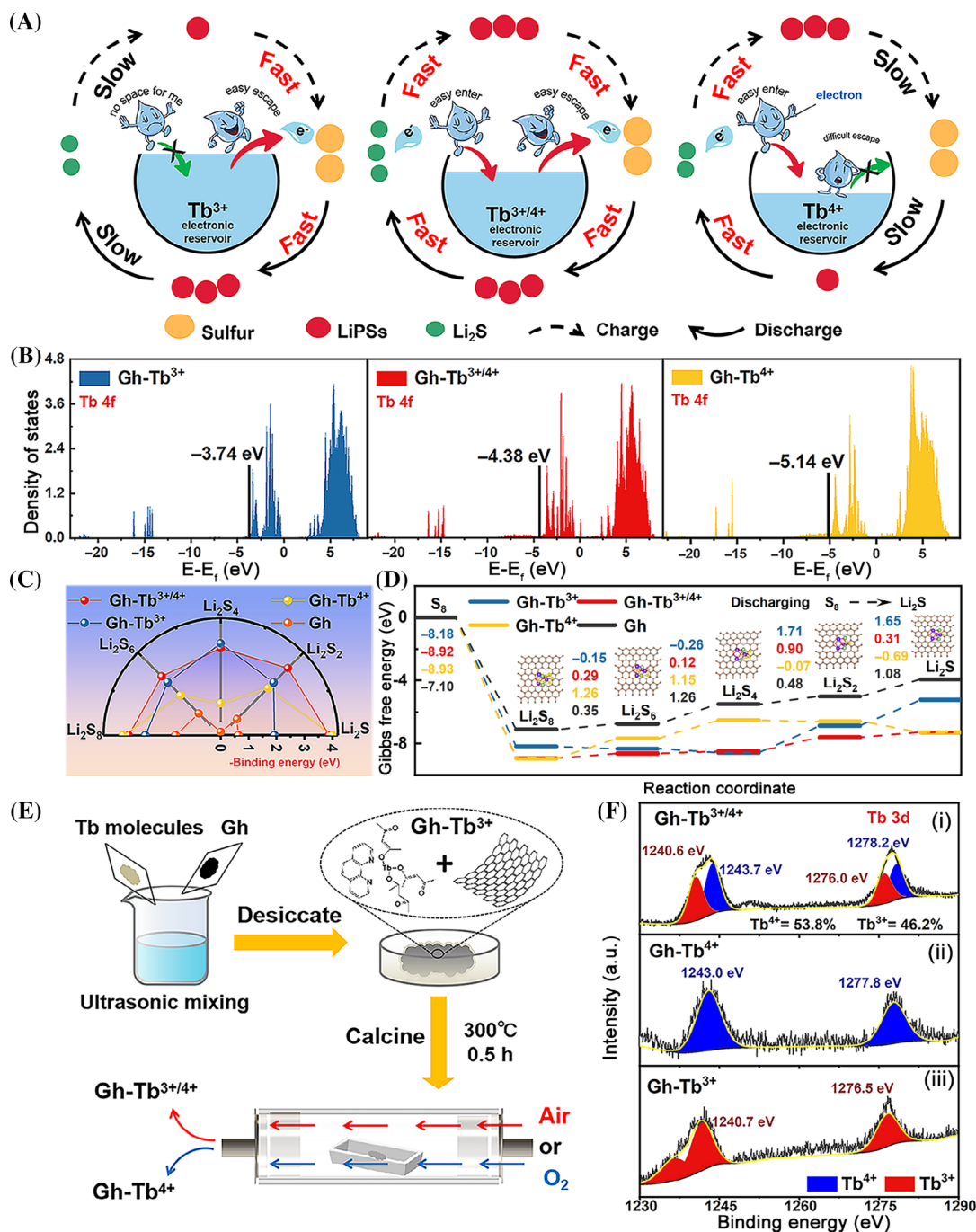


**FIGURE 1** Design, theoretical simulation, and characterization of catalysts and their interaction with LiPSs. (A) Schematic illustration of SRR mechanism on various Tb electronic reservoirs. (B) Density of states of Tb 4f orbitals of  $\text{Gh-Tb}^{x+}$  ( $x = 3, 4, 3+/4$ ) and Gh. (C) The  $E_b$  between substrates ( $\text{Gh-Tb}^{x+}$  ( $x = 3, 4, 3+/4$ ) and Gh) and different LiPSs ( $\text{Li}_2\text{S}_n$ ,  $n = 8, 6, 4, 2, 1$ ). (D) The changes of Gibbs free energy during sulfur reduction reactions on four catalyst surfaces. (E) Schematic illustration of the synthetic procedures for  $\text{Gh-Tb}^{x+}$  ( $x = 3, 4, 3+/4$ ) composites. (F) XPS spectra of Tb 3d performed on  $\text{Gh-Tb}^{x+}$  ( $x = 3, 4, 3+/4$ ).

system, where three Tb valence states were obtained by coordinating 4 Tb atoms with a different number of O atoms (6, 7, and 8 O atoms for  $\text{Tb}^{3+}$ ,  $\text{Tb}^{3+/4+}$ , and  $\text{Tb}^{4+}$ , respectively). As shown in Figure 1B, the relatively higher  $f$ -band center is observed for  $\text{Gh-Tb}^{3+}$ , which implies its capacities in providing electrons to external circuit and stronger absorption to adsorbates by referring

to the  $d$ -electron theory,<sup>26</sup> forming  $\text{Tb}^{3+}$  electron source. Similarly,  $\text{Gh-Tb}^{4+}$  with lower  $f$ -band center is easy to extract electrons from outside and exhibits weak adsorption to adsorbates, forming  $\text{Tb}^{4+}$  electron drain. By contrast,  $\text{Gh-Tb}^{3+/4+}$  possesses the moderate  $f$ -band center of Tb 4f among three composites, indicating its mild adsorption to adsorbed molecules (e.g., LiPSs) and balanced

ability in both gain and loss electrons (i.e., generating electron reservoir (source and drain)). The above  $f$ -band center results are strongly supported by a direct binding energy ( $E_b$ ) calculation between the material and LiPSs. In Figures 1C and S2, it can be seen that the LiPS molecules are adsorbed to Gh-Tb<sup>3+/4+</sup> surfaces by Tb-S bonds, and while the Gh-Tb<sup>3+/4+</sup> generally exhibits the more moderate binding energies to most of LiPSs (Li<sub>2</sub>S<sub>*n*</sub>, *n* = 8, 4, 1) clusters than those of LiPSs over the other three substrates (Gh-Tb<sup>3+</sup>, Gh-Tb<sup>4+</sup>, Gh). That means Gh-Tb<sup>3+/4+</sup> as an electronic reservoir can not only efficiently anchor dissolved sulfur species, but also can favor the following catalytic conversions of LiPSs to a reasonable level.

Furthermore, the possible reaction pathways with Gibbs free energy barrier on the catalyst surfaces were simulated via DFT.<sup>27,28</sup> As shown in Figure 1D, the reduction step of S<sub>8</sub> to Li<sub>2</sub>S<sub>8</sub> shows a spontaneous exothermic reaction on all the substrates. The following two long-chain LiPS reduction steps, from Li<sub>2</sub>S<sub>8</sub> to Li<sub>2</sub>S<sub>4</sub>, are an exothermic reaction for Gh-Tb<sup>3+</sup> and exhibit the smaller positive Gibbs free energy barrier for Gh-Tb<sup>3+/4+</sup> (0.29 eV for Li<sub>2</sub>S<sub>8</sub> to Li<sub>2</sub>S<sub>6</sub>, 0.12 eV for Li<sub>2</sub>S<sub>6</sub> to Li<sub>2</sub>S<sub>4</sub>), while the Gibbs free energy barriers for the formation of short-chain Li<sub>2</sub>S on the surfaces containing Tb<sup>4+</sup> (−0.69 eV for Gh-Tb<sup>4+</sup> and 0.31 eV Gh-Tb<sup>3+/4+</sup>) are much lower than those of Gh-Tb<sup>3+</sup> (1.65 eV) and Gh (1.08 eV), confirming Tb<sup>3+</sup> and Tb<sup>4+</sup> can effectively lower the Gibbs free energy barrier in LCR and SCR, respectively. Considering the generally low Gibbs free energy barrier at each step, in particular the step of Li<sub>2</sub>S<sub>6</sub> to Li<sub>2</sub>S<sub>4</sub> with the lowest value of 0.12 eV, the whole sulfur conversion process from S<sub>8</sub> to Li<sub>2</sub>S is more convenient on Gh-Tb<sup>3+/4+</sup> surface during discharge. From the perspective of electron transfer, we deduce that Tb<sup>3+</sup> electron source may spontaneously donate electrons to long-chain LiPSs, trapping long-chain LiPSs firmly and rapidly converting them to short-chain sulfur species; subsequently, under the driving force of discharge process, as-stored electrons in Tb<sup>4+</sup> electron drain with the properties of weak adsorption but strong catalysis, could be transferred to short-chain sulfur species, facilitating the continuity of sulfur reduction reactions. By virtue of the coexistence of Tb<sup>3+</sup> and Tb<sup>4+</sup>, more efficient electron transfer and electrochemical reactions occur at Tb<sup>3+/4+</sup> electronic reservoir (source and drain).

From the computational studies, it is believed that owing to the moderate  $f$ -band center and duplex electron transfer ability, Tb<sup>3+/4+</sup> electronic reservoir could capture LiPSs more appropriately via the bonding effect by Tb-S bonds without affecting the next smooth LiPS catalytic conversions, thus expecting to improve the electrochemical performance of Li-S batteries.

Guided by the above exciting theoretical calculations, we prepared three Gh-Tb oxides (Gh-Tb<sup>3+</sup>, Gh-Tb<sup>3+/4+</sup>, and Gh-Tb<sup>4+</sup>) and characterized their structures. In the experiments, tris(acetylacetonato)(1,10-phenanthroline) terbium(III) molecules (Figure S3, called as Tb molecules for short below) as the sources of Tb and N were modified onto the conventional Gh using different methods, including physical ultrasonication, high-temperature (300°C, closed to the critical temperature for mass loss, as proved by thermogravimetric analysis (TGA) data in Figure S4 calcining in air or O<sub>2</sub> atmosphere, to form the Gh-Tb<sup>x+</sup> composite with various valences of Tb. The overall synthesis strategy is illustrated schematically in Figure 1E.

The surface compositions of the three Gh-Tb<sup>x+</sup> composites were evaluated by X-ray photoelectron spectroscopy (XPS) analysis. The Tb 3d XPS data for the Gh-Tb<sup>x+</sup> prepared under heat treatment in air conditions (Figure 1Fi) indicates that Tb contributions can be assigned to 46.2% Tb<sup>3+</sup> (1276.0/1240.6 eV) and 53.8% Tb<sup>4+</sup> (1278.2/1243.7 eV),<sup>29–31</sup> which confirms a formation of the mixed-valence Tb, that is, Tb<sup>3+/4+</sup>. By contrast, only Tb<sup>4+</sup> peaks (1277.8/1243.0 eV) dominate the Tb 3d spectrum for the Gh/Tb molecule heated in O<sub>2</sub> atmosphere (Figure 1Fii), suggesting the generation of Gh-Tb<sup>4+</sup>, and Tb<sup>3+</sup> peaks (1276.5/1240.7 eV) appear in the spectrum of the Gh/Tb molecule hybrids without calcination (Figure 1Fiii), namely forming Gh-Tb<sup>3+</sup>. Notably, the presence of pyridinic/pyrrolic N peaks in the N 1s XPS spectra<sup>32–34</sup> for the heat-treated Gh/Tb molecule systems (Gh-Tb<sup>3+/4+</sup>, Gh-Tb<sup>4+</sup>) in Figure S5 suggest a formation of N-doped Gh after the thermal decomposition of Tb molecules containing N element. In order to control the Tb valence as a single variable, a N-doped Gh was employed to prepare the physically mixed Gh-Tb<sup>3+</sup> and Gh reference sample in the following study.

The transmission electron microscope (TEM) images of Gh-Tb<sup>3+</sup> and Gh-Tb<sup>4+</sup> composites show slightly aggregated Tb oxide particles embedded in thin films of Gh (Figure S6A–D), whereas those from Gh-Tb<sup>3+/4+</sup> show evenly distributed Tb oxide particles well covered the whole surface area of Gh (Figure S6E,F). The uniformly dispersed Tb atoms can be distinguished as the brighter spots (Figure S7A) for a close observation on Gh-Tb<sup>3+/4+</sup> composite from aberration-corrected high-angle annular dark-field scanning transmission electron microscopy (HAADF-STEM). The magnified HAADF-STEM image (Figure S7B) suggests that the Tb<sup>3+/4+</sup> oxide species are present in the form of ultra-microclusters. The energy dispersive X-ray spectroscopy (EDX) elemental mappings of the Gh-Tb<sup>3+/4+</sup> hybrid (Figure S8) further confirm the homogeneous coexistence of C, N, O, and Tb elements in the structure, consistent with the XPS results (Figure S9).

Inspired by the characteristics of high conductivity and large active surface area of N-doped Gh, combined with the excellent potential of  $\text{Tb}^{3+/4+}$  with unique electronic structures in adsorption and catalysis of LiPSs, we used Gh-Tb $^{3+/4+}$  as the cathode modification layer of Li-S batteries (Figure S10) to facilitate the SRR kinetics and alleviate the shuttle effect of Li-S batteries.

## 2.2 | Chemical adsorption and LiPS conversion kinetics with Tb electronic reservoir

Surface adsorption of LiPSs constitutes the first important step of heterogeneous electrocatalysis of sulfur conversion reactions. Naturally, a visual LiPS adsorption experiment was conducted by adding an equal amount of Gh (i.e., N-doped Gh), Tb molecules, and Gh-Tb $^{3+/4+}$  hybrids into  $\text{Li}_2\text{S}_6$  solution, respectively, as shown in Figure S11. Apparently, the yellow  $\text{Li}_2\text{S}_6$  solution containing Gh becomes light brown after 12 h of static adsorption (Figure S11ii). This illustrates that besides little adsorption caused by the limited N doping, Gh primarily possesses a certain physical adsorption ability of LiPSs due to its porosity,<sup>35</sup> as probed by the nitrogen adsorption-desorption isotherm results (Figure S12). However, the physical adsorption strength of the host material is too limited to trap LiPSs efficiently. By contrast, the chemical adsorption of Tb molecules has the advantage to anchor abundant LiPSs and promote their subsequent catalytic sulfur conversions, resulting in a pale-yellow solution (Figure S11iii). Due to the synergistic effect of physical and chemical interaction with LiPSs, the color of the  $\text{Li}_2\text{S}_6$  solution turns nearly colorless for the suspension with Gh-Tb $^{3+/4+}$  composites (Figure S11iv), although the specific surface area and mesopore volume of Gh-Tb $^{3+/4+}$  are smaller than those of Gh (Figure S12), confirming the excellent LiPS adsorption capability of Gh-Tb $^{3+/4+}$ .

To further elucidate the intrinsic chemical interactions between Gh-Tb $^{3+/4+}$  and LiPSs, XPS measurements of Gh-Tb $^{3+/4+}$  were implemented before and after adsorption of  $\text{Li}_2\text{S}_6$ . As shown in Figure 2A, pristine Gh-Tb $^{3+/4+}$  exhibits two pairs of deconvoluted Tb 3d peaks located at 1240.4/1275.7 and 1243.2/1277.9 eV belonging to the  $\text{Tb}^{3+}$  and  $\text{Tb}^{4+}$ , respectively.<sup>29–31</sup> After adsorbing  $\text{Li}_2\text{S}_6$ , a significant shift of these peaks toward a higher binding energy ( $\text{Tb}^{3+}$  at 1240.6/1276.1 eV and  $\text{Tb}^{4+}$  at 1243.8/1278.5 eV) can be perceived, suggesting a reduction in the electron cloud density of Tb atoms. In the XPS spectra of S 2p (Figure 2B), a pair of peaks display at the high binding energy region between 168 and 172 eV, corresponding to the sulfate species formed by

the oxidation of sulfur in air.<sup>36,37</sup> In contrast, Gh-Tb $^{3+/4+}$  composites could demonstrate stronger intensity response for S-S bond at 164.1/165.2 eV<sup>33,38</sup> and two additional peaks located at 162.6/163.7 eV, which can be assigned to the S-Metal (S-M) bond.<sup>39,40</sup> All above results imply good chemical affinity of Gh-Tb $^{3+/4+}$  to LiPSs via Tb-S bond, as proved by the DFT results in Figure S2. Meanwhile, the interactive chemistry between Gh-Tb $^{3+/4+}$  and LiPSs can also be confirmed by the Li 1s XPS spectra (Figure S13), in which the emergence of stronger Li...N bond at 54.5 eV further demonstrates the “lithium-bond”-like configuration<sup>41</sup> formed between N-doped Gh and LiPSs. Our DFT data in Figure S2 also support the formation of lithium-bond, where Li atoms of the distorted LiPSs are adjacent to N atoms of Gh.

Collectively, the formation of Tb-S and N...Li bonds between Gh-Tb $^{3+/4+}$  and LiPSs is highly beneficial to the superior LiPS chemical confinement toward efficient shuttle inhibition, in agreement with the binding energy calculations (Figure 1C). Based on this good prerequisite, the LiPS conversion kinetics, including liquid-liquid and liquid-solid conversions, was deeply investigated on carbon nanotubes-sulfur (CNTs-S)/Gh-Tb $^{3+/4+}$  cathode by comparing with other cathodes.

The catalytic kinetics regarding the initial liquid-liquid conversion process between dissolved LiPSs ( $\text{Li}_2\text{S}_n$ ,  $4 \leq n \leq 8$ ) was evaluated via symmetric cell techniques using identical pairs of electrodes (CNTs/Gh-Tb $^{3+/4+}$ , CNTs/Gh-Tb $^{4+}$ , CNTs/Gh-Tb $^{3+}$ , or CNTs/Gh) and a  $\text{Li}_2\text{S}_6$  electrolyte. All the cyclic voltammetry (CV) curves of Tb-containing cells at the scan rate of  $30 \text{ mV s}^{-1}$  display two pairs of redox peaks ( $a/a_0$  and  $b/b_0$ ), demonstrating reliable electrocatalytic activity of Tb oxides toward LiPS conversion (Figure 2C).<sup>42</sup> The CNTs/Gh-Tb $^{3+}$  symmetric cell gives more positive reduction peak due to sulfur to  $\text{Li}_2\text{S}_6$  ( $-0.05 \text{ V}$ ) and more negative oxidation peak due to  $\text{Li}_2\text{S}_6$  to  $\text{S}_8$  ( $0.54 \text{ V}$ ) than CNTs/Gh-Tb $^{4+}$  symmetric cell ( $-0.07 \text{ V}$  for reduction/ $0.56 \text{ V}$  for oxidation), indicating the superiority of  $\text{Tb}^{3+}$  in promoting liquid long-chain LiPS conversion.<sup>15</sup> Of note, the smallest reaction polarization, the highest redox current response and the most distinct redox peaks on CNTs/Gh-Tb $^{3+/4+}$  electrode substantiate that the *f* orbital engineering indeed brings about robust activity to electrocatalyze soluble LiPS within the liquid phase.<sup>28</sup> Similar results are also demonstrated in electrochemical impedance spectroscopy (EIS) of the symmetric cells. As shown in Figure S14, the symmetric cells with  $\text{Tb}^{3+}$  (CNTs/Gh-Tb $^{3+/4+}$ , CNTs/Gh-Tb $^{3+}$ ) clearly exhibit a lower charge transfer resistance ( $R_{ct}$ , Table S1) than the other two cells, specially CNTs/Gh-Tb $^{3+/4+}$  symmetric cell has the lowest  $R_{ct}$ , suggesting its fast charge transfer and facilitated SRR.<sup>43</sup>

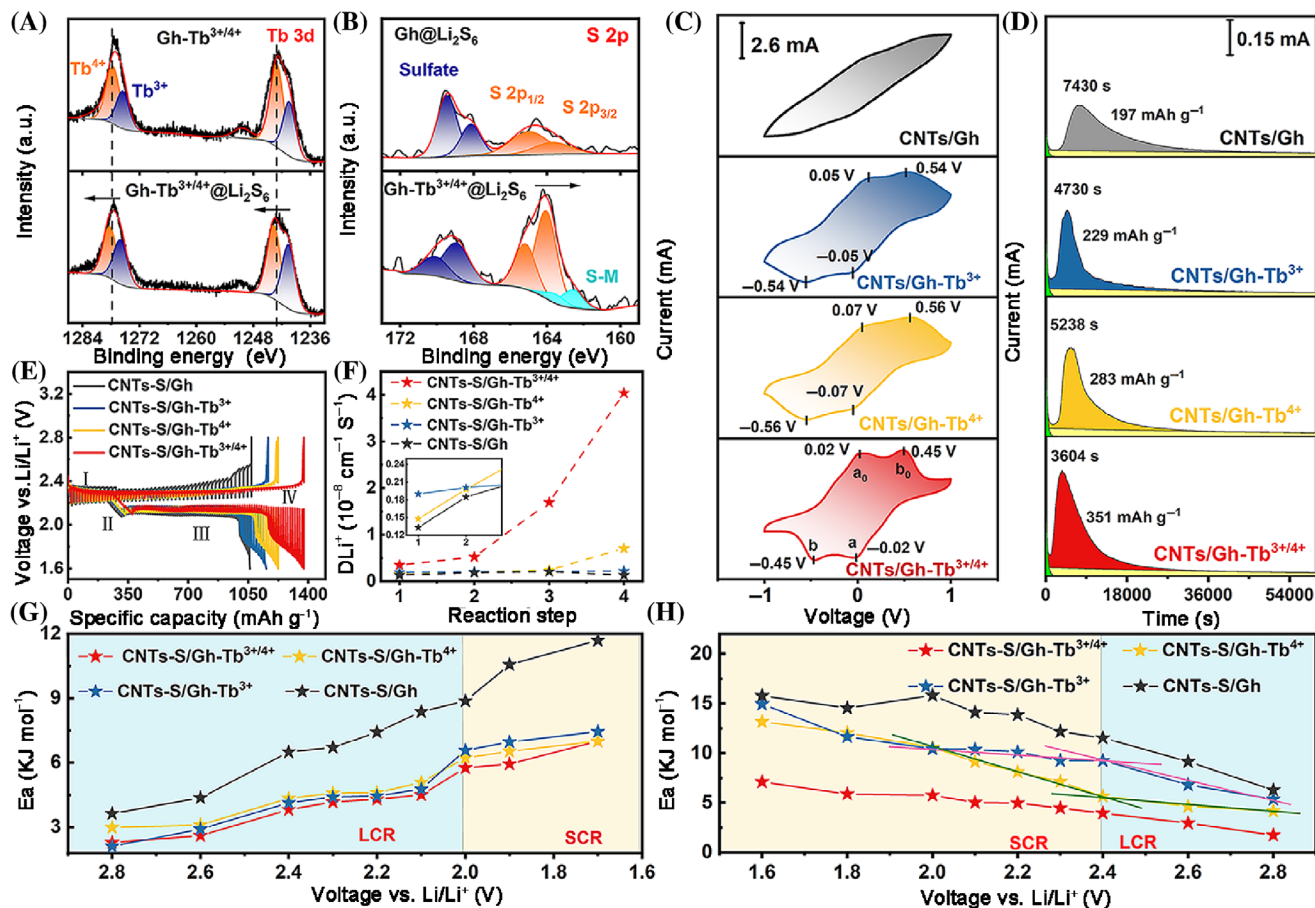


**FIGURE 2** Adsorption and kinetics evaluations on the multiphase SRR. (A) High-resolution Tb 3d XPS spectra of Gh-Tb<sup>3+/4+</sup> before and after Li<sub>2</sub>S<sub>6</sub> adsorption. (B) S 2p XPS spectra of Gh and Gh-Tb<sup>3+/4+</sup> after interacting with Li<sub>2</sub>S<sub>6</sub>. (C) CV curves of symmetric cells using Li<sub>2</sub>S<sub>6</sub> electrolyte as active component and CNTs/Gh-Tb<sup>x+</sup> ( $x = 3, 4, 3+/4$ ) and CNTs/Gh as electrodes at 30 mV s<sup>-1</sup>. (D) Potentiostatic discharge curves of Li<sub>2</sub>S deposition on CNTs/Gh-Tb<sup>x+</sup> ( $x = 3, 4, 3+/4$ ) and CNTs/Gh cathodes, respectively. The regions with light yellow and green represent the reduction of Li<sub>2</sub>S<sub>8</sub> and Li<sub>2</sub>S<sub>6</sub>, respectively. The precipitation of Li<sub>2</sub>S is indicated by gray, blue, yellow, or red color. (E) Charge/discharge curves of the GITT test during the second cycle for CNTs-S/Gh-Tb<sup>x+</sup> ( $x = 3, 4, 3+/4$ ) and CNTs-S/Gh cathodes (current pulse: 83.7 mA g<sup>-1</sup>, pulse for 10 min, 2 h relaxation). (F)  $D_{Li^+}$  of the four cathodes at each reaction step. Activation energy profiles for the SRR process among four cathodes at various voltages of (G) discharge and (H) charge.

Besides, a potentiostatic nucleation/dissolution experiment affords vital evidences on the kinetic promotion for liquid–solid transition pertaining to Li<sub>2</sub>S deposition/dissociation. To probe the liquid–solid transition from LiPSs (Li<sub>2</sub>S<sub>*n*</sub>,  $n < 4$ ) to Li<sub>2</sub>S, the potentiostatic nucleation experiments were conducted at 2.04 V using the coin cells with Li<sub>2</sub>S<sub>8</sub> electrolyte. According to Faraday's law, the specific capacity of Li<sub>2</sub>S precipitation was calculated and presented in the  $I-t$  curves (see Figure 2D for details). Specifically, the CNTs/Gh-Tb<sup>3+/4+</sup> cathode describes a faster responsiveness of Li<sub>2</sub>S nucleation (3604 s), higher current density (0.45 mA) and larger Li<sub>2</sub>S precipitation capacity (351 mAh g<sup>-1</sup>) than the other three cathodes (0.37 mA, 283 mAh g<sup>-1</sup> at 5238 s for CNTs/Gh-Tb<sup>4+</sup>; 0.36 mA, 229 mAh g<sup>-1</sup> at 4730 s for CNTs/Gh-Tb<sup>3+</sup>; 0.22 mA, 197 mAh g<sup>-1</sup> at 7430 s for CNTs/Gh), pointing to accelerated Li<sub>2</sub>S deposition kinetics on CNTs/Gh-

Tb<sup>3+/4+</sup> surface. After the Li<sub>2</sub>S deposition, the anodic process from Li<sub>2</sub>S to LiPSs (Li<sub>2</sub>S<sub>*n*</sub>,  $4 \leq n \leq 8$ ), that is, Li<sub>2</sub>S dissolution, was also investigated by potentiostatically charging the cells at 2.35 V. As exhibited in Figure S15, a much earlier (7864 s) and larger oxidation peak current (0.6 mA) and a higher amount of Li<sub>2</sub>S decomposition (corresponding to 621 mAh g<sup>-1</sup>) on CNTs/Gh-Tb<sup>3+/4+</sup> than other control electrodes (0.55 mA, 586 mAh g<sup>-1</sup> at 7575 s for CNTs/Gh-Tb<sup>4+</sup>; 0.36 mA, 397 mAh g<sup>-1</sup> at 8800 s for CNTs/Gh-Tb<sup>3+</sup>; 0.19 mA, 327 mAh g<sup>-1</sup> at 14259 s for CNTs/Gh) represent the best catalytical capability of Tb<sup>3+/4+</sup> to enhance Li<sub>2</sub>S oxidation kinetics.<sup>32</sup> It is important to recognize that CNTs/Gh-Tb<sup>4+</sup> cathode presents the second-best properties during both Li<sub>2</sub>S deposition and decomposition, implying Tb<sup>4+</sup> is good at boosting the short-chain LiPS conversion (liquid–solid conversion).

Such an analogous result is also verified by the potentiostatic intermittent titration technique (PITT) and galvanostatic intermittent titration technique (GITT), which were conducted in practical working Li-S batteries but not in an ideal  $\text{Li}_2\text{S}_8$  solution. In PITT experiments, the assembled cells were potentiostatically discharged from open voltage to 1.6 V with an interval of 2 mV. Figure S16 shows the current response versus voltage pulses. At titration potentials above 2.1 V, the sharp current responses increased by  $\sim 153.6\%$  are discerned at each potentiostatic step with  $\text{Tb}^{3+/4+}$  added, followed by rapid current drops in a very short time ( $\sim 16$  s), suggesting the presence of  $\text{Tb}^{3+/4+}$  alters the electrochemical equilibrium and improves the liquid-liquid conversion kinetics.<sup>44</sup> The deposition behaviors of  $\text{Li}_2\text{S}$  on cathode surface were probed between 2.1 and 2.0 V. Obviously, the CNTs-S/Gh-Tb<sup>3+/4+</sup> cell reaches the maximum current density of  $0.41 \text{ mA cm}^{-2}$  (52% higher than that of  $0.27 \text{ mA cm}^{-2}$  in CNTs-S/Gh cell) ahead of the CNTs-S/Gh cell due to a faster deposition rate. The  $\text{Li}_2\text{S}$  deposition capacity of CNTs-S/Gh-Tb<sup>3+/4+</sup> ( $705.3 \text{ mAh g}^{-1}$ ) is 1.16 times as much as that of the control sample ( $607.3 \text{ mAh g}^{-1}$ ), again indicating the similar kinetic advantage of CNTs-S/Gh-Tb<sup>3+/4+</sup> in the liquid-solid conversion.

The GITT was further adopted to monitor the  $\text{Li}^+$  transport behavior, which is a key descriptor affecting the liquid-solid conversion kinetics.<sup>45,46</sup> As seen in Figure 2E, the discharge curves of the Li-S batteries with CNTs-S/Gh-Tb<sup>3+/4+</sup> cathode under the GITT mode show much longer second platform and smaller potential fluctuation, especially in region III ( $\sim 2.1$  V) relating to the conversion from soluble LiPSs to solid  $\text{Li}_2\text{S}_2/\text{Li}_2\text{S}$ , during the discharge process compared with other three cathodes. For the GITT profiles during charge, a large potential fluctuation is observed at the initial solid-solid conversion process (from  $\text{Li}_2\text{S}$  to  $\text{Li}_2\text{S}_2$ ) with slow kinetics at all cathodes, but it decreases the most at CNTs-S/Gh-Tb<sup>3+/4+</sup> cathode due to solid-liquid conversion and keeps at a small overpotential in liquid-liquid conversion. Furthermore, the  $\text{Li}^+$  diffusion coefficients ( $D_{\text{Li}^+}$ ) of the cells were calculated according to Fick's second law, as given in Equation (1).

$$D_{\text{Li}^+} = \frac{4}{\pi\tau} \left( \frac{m_B V_M}{M_B A} \right)^2 \left( \frac{\Delta E_s}{\Delta E_\tau} \right)^2 \quad (1)$$

where  $m_B$ ,  $V_M$ , and  $M_B$  are the mass, molar volume, and molecular weight of cathode material, respectively;  $\tau$  is the duration of the current pulse (600 s) and  $A$  is the surface area of active material.  $\Delta E_s$  is the change of the steady-state voltage due to the current pulse;  $\Delta E_\tau$  is the voltage change during the constant current pulse.<sup>47,48</sup>

As illustrated in Figure 2F, where the elevated  $D_{\text{Li}^+}$  to an order of magnitude for CNTs-S/Gh-Tb<sup>3+/4+</sup>-based cell confirms the best function of CNTs-S/Gh-Tb<sup>3+/4+</sup> in promoting  $\text{Li}^+$  diffusion and activating the lithiation kinetics, especially from liquid  $\text{Li}_2\text{S}_4$  to solid  $\text{Li}_2\text{S}_2/\text{Li}_2\text{S}$ . What's more, the  $D_{\text{Li}^+}$  of CNTs-S/Gh-Tb<sup>3+</sup> is larger than that of CNTs-S/Gh-Tb<sup>4+</sup> at step I and II, conversely the smaller  $D_{\text{Li}^+}$  of CNTs-S/Gh-Tb<sup>3+</sup> than that of CNTs-S/Gh-Tb<sup>4+</sup> is observed for step III and IV, confirming the positive function of  $\text{Tb}^{3+}$  and  $\text{Tb}^{4+}$  in liquid-liquid conversion (long-chain LiPS conversion) and liquid-solid conversion (short-chain LiPS conversion), respectively.

The above sulfur redox reaction kinetics involving the liquid-liquid and liquid-solid conversions can be directly and fundamentally represented by the apparent activation energy ( $E_a$ ),<sup>49</sup> which was calculated through experimentally determining EIS spectra at various voltages and temperatures (Figures S17–S24) and their analysis (Figure S25) after fitting with the equivalent circuit in Figure S26. During discharge process (Figure 2G),  $E_a$  displays a low value at the easy long-chain LiPS forming step (2.8–2.4 V) and gradually increases at the short-chain LiPS forming step (2.4–2.1 V), finally reaching a maximum value at the most difficult insoluble product forming step (2.0–1.7 V). A reverse change tendency of  $E_a$  can be seen clearly during charge process (Figure 2H). Remarkably, over the entire discharge process, the  $E_a$  of  $\text{Tb}^{3+}$  sample is lower than that of  $\text{Tb}^{4+}$  sample in the long-chain LiPS conversion voltage region (2.8–2.1 V), and  $\text{Tb}^{4+}$  sample has lower  $E_a$  in the low voltage range of short-chain LiPS conversion. Similar results are demonstrated in charge process, where a relatively low  $E_a$  with a larger change rate for CNTs-S/Gh-Tb<sup>4+</sup> cathode in short-chain LiPS conversion voltage (around 2.3 V) and an increased change rate of  $E_a$  for CNTs-S/Gh-Tb<sup>3+</sup> cathode in long-chain LiPS conversion voltage (after 2.4 V) are observed. The above results again show the function of  $\text{Tb}^{3+}$  and  $\text{Tb}^{4+}$  in promoting the long-chain and short-chain LiPS conversion, respectively. Besides, in contrast to the counterparts, the overall value of  $E_a$  decreases at each step of discharge/charge processes with the addition of  $\text{Tb}^{3+/4+}$ , once again revealing that the  $\text{Tb}^{3+/4+}$  can lower the energy barriers and significantly expedite the dual-directional sulfur conversion kinetics accompanied by markedly increased capacity, which is expected to improve the battery performance.

### 2.3 | The exploration of unique role of Tb electronic reservoir in Li-S chemistry

A semi-in situ XPS study was carried out to confirm the working mechanisms of different catalysts. As shown in

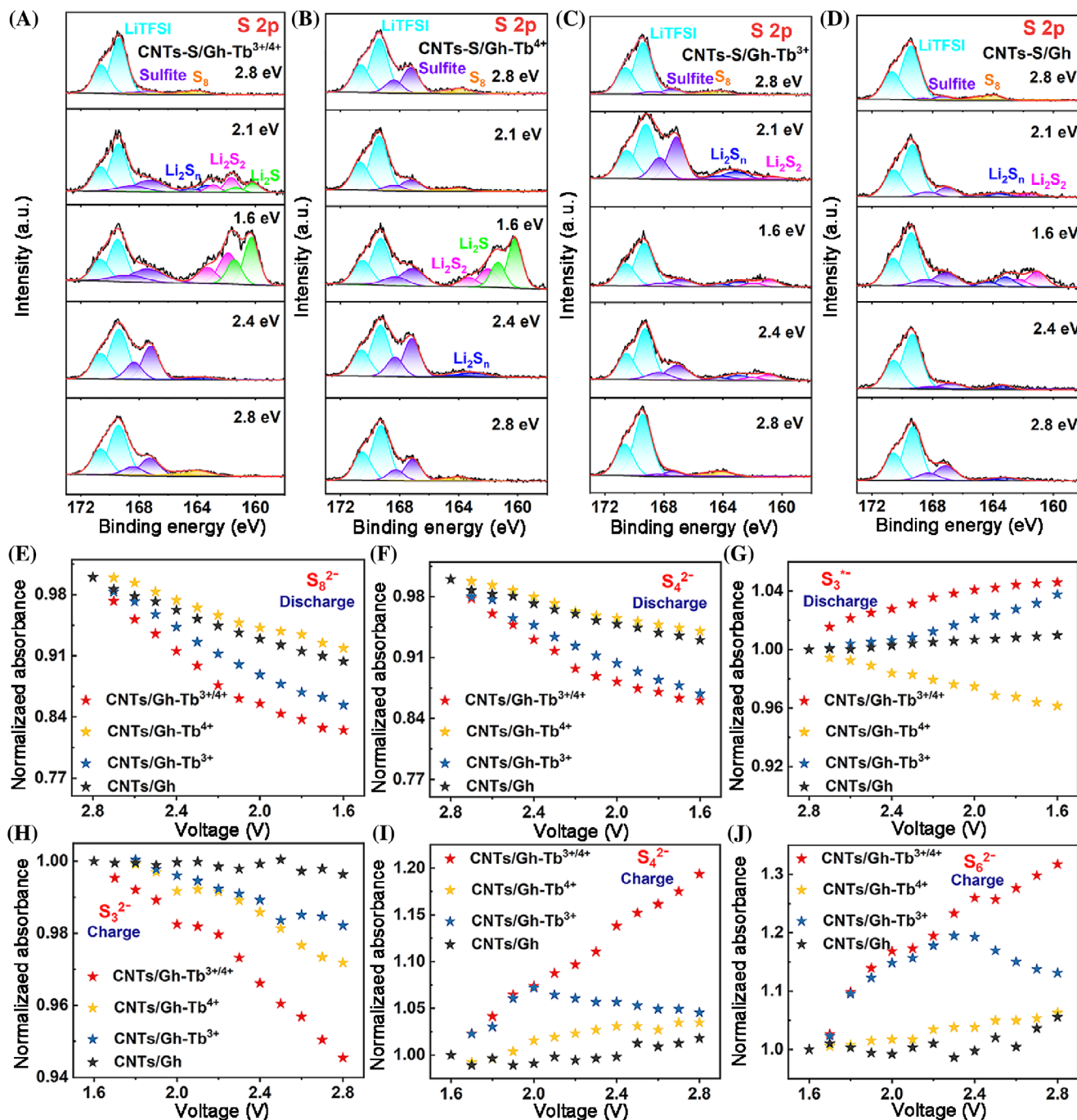


**FIGURE 3** Catalytic functions of the Tb electronic reservoirs toward LiPSs. Semi-in situ S 2p XPS spectra of (A) CNTs-S/Gh-Tb<sup>3+/4+</sup>, (B) CNTs-S/Gh-Tb<sup>4+</sup>, (C) CNTs-S/Gh-Tb<sup>3+</sup>, and (D) CNTs-S/Gh cathodes after discharging and charging to specific states. The normalized absorbance of sulfur species in Li<sub>2</sub>S<sub>8</sub> solution on CNTs/Gh-Tb<sup>3+/4+</sup>, CNTs/Gh-Tb<sup>4+</sup>, CNTs/Gh-Tb<sup>3+</sup>, and CNTs/Gh during (E–G) discharge and (H–J) charge.

Figure 3A–D, S 2p signals at 169.4/170.6 eV and 167.2/168.6 eV are the characteristic peaks of salt lithium bis(trifluoromethanesulfonyl)imide (LiTFSI) and sulfite from the decomposition of LiTFSI, according to literature reports.<sup>6,36</sup> Deconvolution of S 2p spectra under the low binding energies gives four unique components, namely, S<sub>8</sub> at 164.0/165.3 eV, long-chain LiPSs (Li<sub>2</sub>S<sub>n</sub>, 4 ≤ n ≤ 8)

at 163.3/164.4 eV along with short-chain Li<sub>2</sub>S<sub>2</sub> and Li<sub>2</sub>S at 161.7 and 160.2 eV,<sup>37,41</sup> respectively. Based on the intensity evolution of different sulfur species during cycling, we can analyze sulfur catalytic conversion with different catalyst. At fully charged state (2.8 V), the surface components of all the cathodes are predominantly S<sub>8</sub>. Interestingly, when the cells were galvanostatically discharged to

2.0 V, a significant decrease in  $S_8$  signals and a considerable enhancement in long-chain LiPSs ( $Li_2S_n$ ,  $4 \leq n \leq 8$ ) are observed in the cathodes containing  $Tb^{3+}$  (CNTs-S/Gh- $Tb^{3+/4+}$  and CNTs-S/Gh- $Tb^{3+}$ ), implying the good catalytic effect of  $Tb^{3+}$  on the conversion from  $S_8$  to long-chain LiPSs. At the end of discharge (1.6 V), the cathodes with  $Tb^{4+}$  (CNTs-S/Gh- $Tb^{3+/4+}$  and CNTs-S/Gh- $Tb^{4+}$ ) reveal stronger intensities of  $Li_2S_2/Li_2S$  peaks than the  $Tb^{4+}$ -free cathodes (CNTs-S/Gh- $Tb^{3+}$  and CNTs-S/Gh), and few long-chain LiPSs ( $Li_2S_n$ ,  $4 \leq n \leq 8$ ) are left in  $Tb^{4+}$ -containing cathodes, suggesting  $Tb^{4+}$  can catalyze the conversion from long-chain LiPSs to short-chain  $Li_2S_2/Li_2S$ . This phenomenon is highly reversible during a charge process. As shown in Figure 3A–D, after charging to 2.4 V, short-chain  $Li_2S_2/Li_2S$  are more easily converted to long-chain LiPSs ( $Li_2S_n$ ,  $4 \leq n \leq 8$ ) in the cathodes with  $Tb^{4+}$  (CNTs-S/Gh- $Tb^{3+/4+}$  and CNTs-S/Gh- $Tb^{4+}$ ), while a more efficient conversion of long-chain LiPSs ( $Li_2S_n$ ,  $4 \leq n \leq 8$ ) to  $S_8$  can be found in the cathodes containing  $Tb^{3+}$  (CNTs-S/Gh- $Tb^{3+/4+}$  and CNTs-S/Gh- $Tb^{3+}$ ) as the cells are charging to 2.8 V. Upon the electronic structure coupling and synergetic catalytic effect of  $Tb^{3+}$  and  $Tb^{4+}$ , the CNTs-S/Gh- $Tb^{3+/4+}$  cathode exhibits the optimum signals of sulfur species at each discharge/charge state, manifesting its extraordinary ability to catalyze the consecutive LiPS conversion.

This statement can be further supported by in situ UV-vis spectra at electrode/electrolyte interface (Figures S27 and S28) and their corresponding qualitative

analysis of absorbance intensity (Figure 3E–J), which reveals a faster decrease in  $S_8^{2-}/S_4^{2-}$  intensity accompanied by a higher increase in  $S_3^{*-}$  radical signal during discharge for  $Tb^{3+}$ -containing cathodes (CNTs/Gh- $Tb^{3+/4+}$  and CNTs/Gh- $Tb^{3+}$ ) compared with those for  $Tb^{3+}$ -free cathodes (CNTs/Gh- $Tb^{4+}$  and CNTs/Gh), confirming  $Tb^{3+}$  is more inclined to accelerate the conversion between long-chain LiPSs to short-chain LiPSs. This is further demonstrated by the decreased change in  $S_4^{2-}/S_6^{2-}$  signal for CNTs/Gh- $Tb^{3+}$  cathode upon charging from  $\sim 2.3$  to 2.8 V. It is noteworthy that, the absorbance intensity of CNTs/Gh- $Tb^{4+}$  cathode toward  $S_3^{*-}$  radicals continuously declines upon discharging, while the intensity value of the cathodes with  $Tb^{4+}$  (CNTs/Gh- $Tb^{3+/4+}$  and CNTs/Gh- $Tb^{4+}$ ) shows a faster decrease toward  $S_3^{2-}$  but an increase toward  $S_4^{2-}/S_6^{2-}$  as the charge proceeds, again suggesting  $Tb^{4+}$  can boost the conversion of short-chain LiPSs. Thus, the best conversion of CNTs/Gh- $Tb^{3+/4+}$  toward both long-chain and short-chain LiPSs during discharge/charge boils down to the electronic structure coupling of  $Tb^{3+}$  and  $Tb^{4+}$  once again.

To attain an in-depth understanding of the reasons for the improved reaction kinetics of the CNTs-S/Gh- $Tb^{3+/4+}$  cathodes, the transformation pathways of LiPSs on various sulfur cathodes were analyzed by in situ Raman spectroscopy in real-time. At the initial discharge state (2.8 V), there are three distinctive peaks located at 154, 219, and 473  $cm^{-1}$  for  $S_8$  species on CNTs-S/Gh cathode surface in Figure 4A,B, where the intensities of

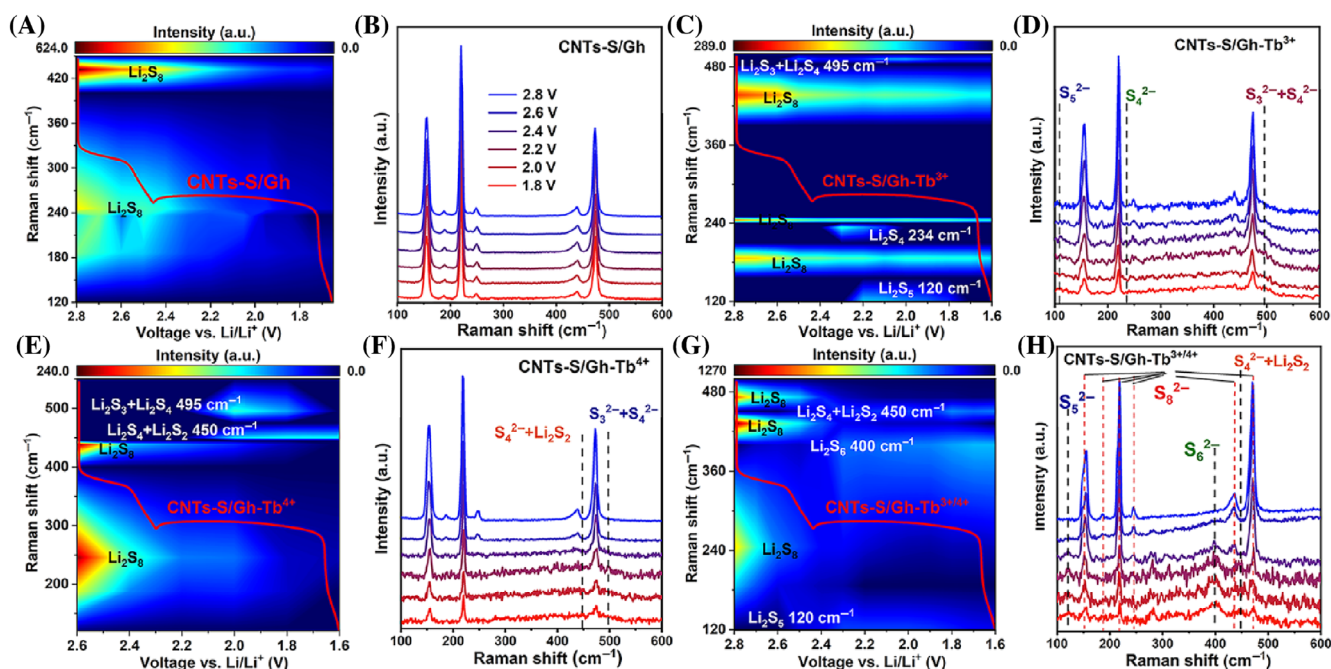


FIGURE 4 Transformation pathways of LiPSs on various cathodes. In situ Raman spectra and the corresponding contour profiles of (A,B) CNTs-S/Gh- $Tb^{3+/4+}$ , (C,D) CNTs-S/Gh- $Tb^{3+}$ , (E,F) CNTs-S/Gh- $Tb^{4+}$ , and (G,H) CNTs-S/Gh electrodes during discharge.

$S_8$  peaks gradually decrease as the electrode is fully discharged to 1.6 V. However, there is no any signal indicating the generation of short-chain LiPSs during the whole processes, owing to the inappreciable catalytic ability of CNTs-S/Gh. For CNTs-S/Gh-Tb<sup>3+</sup> (Figure 4C,D) and CNTs-S/Gh-Tb<sup>4+</sup> cathodes (Figure 4E,F), in situ Raman spectroscopy shows similar  $S_8$  conversion. In addition, two weak peaks at 120 and 495 cm<sup>-1</sup>, corresponding to  $S_5^{2-}$  and  $S_3^{2-} + S_4^{2-}$  signals, respectively, are observed at around 2.2 V on CNTs-S/Gh-Tb<sup>3+</sup> cathode, while the emerge of  $S_4^{2-} + Li_2S_2$  signal at 450 cm<sup>-1</sup> at the end of discharge (2.1–2.0 V) for CNTs-S/Gh-Tb<sup>4+</sup> cathode, representing the roles of Tb<sup>3+</sup> and Tb<sup>4+</sup> in promoting the conversion of long-chain and short-chain LiPSs, respectively. For the CNTs-S/Gh-Tb<sup>3+/4+</sup> cathode (Figure 4G,H), besides a similar trend of  $S_8$ , Raman signals of  $S_4^{2-} + Li_2S_2$  emerge with obvious  $S_6^{2-}$  and  $S_5^{2-}$  signals in the middle of discharge (from 2.3 to 2.2 V), following by the decreases of  $S_6^{2-}$  and  $S_5^{2-}$  and increase of  $Li_2S_2$  at the end of discharge, suggesting a sufficient and distinctive sulfur conversion pathway from  $S_8$  to  $Li_2S/Li_2S_2$  through the intermediate state of  $S_6^{2-}/S_5^{2-}/S_4^{2-}$  species. The lowest Gibbs free energy barrier at the step of  $Li_2S_6$  to  $Li_2S_4$  in DFT calculations (Figure 1D) is probably due to the formation of the new  $Li_2S_5$  intermediate, which can be a springboard between  $Li_2S_6$  and  $Li_2S_4$ .

## 2.4 | Electrochemical energy storage evaluation of the Tb electronic reservoir in Li-S batteries

The catalytic efficacy of *f* orbital engineering scenario in practical Li-S batteries was further validated with electrochemical characterizations. A 78 wt% sulfur content is revealed by thermogravimetric analysis (Figure S29). It is worth mentioning that the catalyst loading was controlled as low as 0.7 wt% to avoid influencing the sulfur content of the cathode. Moreover, the mass ratio of catalyst to Gh was 1:10 in the cathode is proved to be optimum for the battery performance (Figure S30). The Li-S cells with a routine sulfur loading of ~1.0 mg cm<sup>-2</sup> were first evaluated.

From the CV plots of the four cells in Figures S31 and 5A, there are two major reduction peaks around 2.3 and 2.0 V during discharge process, corresponding to the two-step redox reaction from  $S_8$  to long-chain LiPSs ( $Li_2S_n$ ,  $4 \leq n \leq 8$ , P<sub>1</sub>) then to short-chain  $Li_2S_2/Li_2S$  (P<sub>2</sub>) as reported previously.<sup>50</sup> Besides, the broad continuous oxidation peaks at ~2.4 V during charge process are ascribed to the oxidation from  $Li_2S_2/Li_2S$  to LiPSs (P<sub>3</sub>) and further to  $S_8$  (P<sub>4</sub>). The CV curves of the CNTs-S/Gh-Tb<sup>3+/4+</sup> cells are almost overlapping after the initial cycle, which means

a better reversibility of the cell reactions. The separation between P<sub>2</sub> and P<sub>3</sub> peaks of CNTs-S/Gh-Tb<sup>3+/4+</sup> cell is minimum, in comparison with that of CNTs-S/Gh-Tb<sup>4+</sup>, CNTs-S/Gh-Tb<sup>3+</sup>, and CNTs-S/Gh cells (Figure S32), implying the minimum electrochemical polarization and the best electrochemical kinetics of batteries. Impressively, the most positive cathodic reaction potential and the most negative anodic reaction potential of CNTs-S/Gh-Tb<sup>3+/4+</sup> cell suggest CNTs-S/Gh-Tb<sup>3+/4+</sup> cell has the lowest energy barrier to the sulfur conversion and the lowest redox reaction resistance among the four cells, matching well with the activation energy results (Figure 2G,H) and electrochemical impedance spectroscopy (EIS) analysis data (Figures S33 and S34), in which CNTs-S/Gh-Tb<sup>3+/4+</sup> cell displays the lowest charge transfer resistance ( $R_{ct}$ , Figure S33) and electrolyte resistance ( $R_e$ , the details are given in Figure S34) compared with the other cells.

To quantitatively evaluate the catalytic effect on sulfur conversion kinetics, Tafel slopes were calculated based on the reduction and oxidation peaks in the CV profiles. As illustrated in Figures 5B,C and S35, the Tafel slopes for P<sub>1</sub>, P<sub>2</sub>, and P<sub>3</sub> peaks decrease from 107, 99, and 103 mV dec<sup>-1</sup> on the CNTs-S/Gh cathode to 96, 91, and 76 mV dec<sup>-1</sup> on the CNTs-S/Gh-Tb<sup>3+</sup> cathode and to 72, 59, and 65 mV dec<sup>-1</sup> on the CNTs-S/Gh-Tb<sup>4+</sup> cathode, respectively. Importantly, incorporation of Tb<sup>3+/4+</sup> further decreases the Tafel slopes for the peaks to the lowest values (65, 42, and 60 mV dec<sup>-1</sup> for P<sub>1</sub>, P<sub>2</sub>, and P<sub>3</sub> peaks, respectively), signifying a 42%–60% electrokinetic enhancement in each sulfur redox step endowed by selectively accelerate engineering.

According to the galvanostatic discharge/charge profiles at different rates in Figures 5D and S36, two plateaus in discharge and charge curves correspond to the reduction and oxidation reaction processes of Li-S batteries,<sup>12</sup> coinciding well with the redox peaks in CV results (Figure 5A). Notably, the stable discharge/charge behaviors without aggravated polarization can be observed at a relatively high rate (2 C), due to faster electronic/ionic transport for LiPS conversion. Take the second cycle curves at 0.2 C as an example for in-depth analysis (Figure 5D), the smallest voltage polarization ( $\Delta E = 180$  mV, Figure S37) represented by the gap between the discharge and charge curves, the  $Q_{up}$  capacity value of 392 mAh g<sup>-1</sup> approached the theoretical capacity (418 mAh g<sup>-1</sup>) at the first plateau around 2.3 V (Figure S38), an extended second plateau ( $Q_{low}$ ) by 24% involving  $Li_2S$  deposition and the lowest onset potential (0.24 V) to produce more LiPSs for the CNTs-S/Gh-Tb<sup>3+/4+</sup> cell can be identified compared with the other three cells, which implies the higher utilization of active sulfur and fast liquid-liquid conversion, the accelerated kinetics of  $Li_2S$  nucleation/deposition and

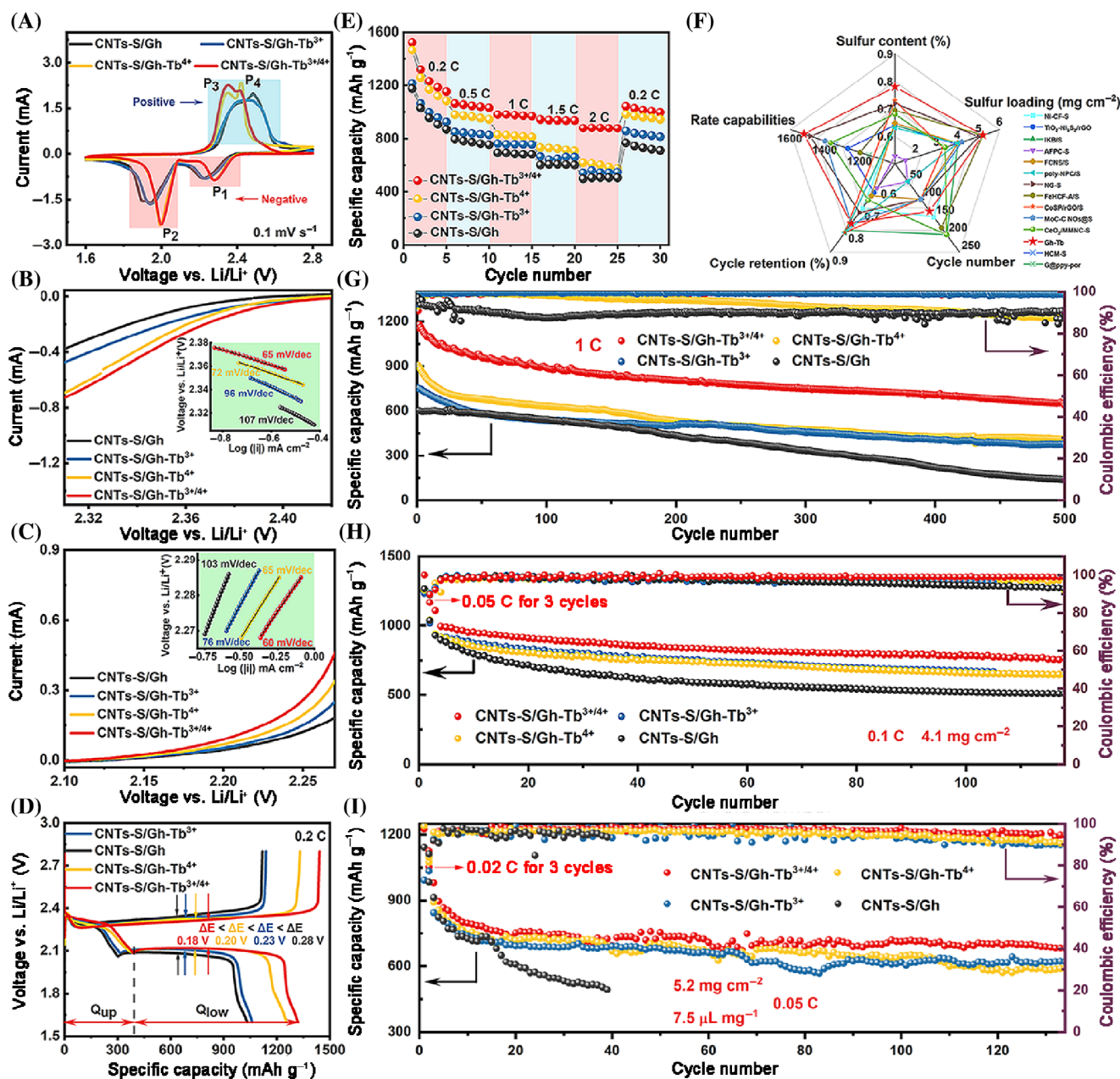


**FIGURE 5** Electrochemical performance toward Li-S batteries. (A) CV curves of different cathodes at  $0.1 \text{ mV s}^{-1}$ . The Tafel slopes of the cathodic and anodic processes obtained from the CVs in Figure 5A, corresponding to (B) P<sub>1</sub> and (C) P<sub>3</sub>. (D) Galvanostatic discharge/charge profiles at 0.2 C of Li-S coin cells with different cathodes for the second cycle. (E) Rate capabilities varied from 0.2 C to 2 C of Li-S coin cells with different cathodes. (F) Performance comparison between CNTs-S/Gh-Tb<sup>3+/4+</sup> electrode and others electrode systems in Table S2. (G) Long-term cycling performance at 1 C of Li-S coin cells with different cathodes. (H) Cycling performance of as-prepared Li-S cells with a high sulfur loading of  $4.1 \text{ mg cm}^{-2}$  at 0.1 C. (I) Cycling performance of the four Li-S cells with a high sulfur loading of  $5.2 \text{ mg cm}^{-2}$  and a E/S ratio of  $7.5 \text{ } \mu\text{L mg}^{-1}$  at 0.05 C after an activation process of 3 cycles at 0.02 C.

liquid–solid conversion by the extraordinary catalysis of Gh-Tb<sup>3+/4+</sup>.

As expected, the CNTs-S/Gh-Tb<sup>3+/4+</sup> cell exhibits the best rate abilities (Figure 5E). Not only superior discharge capacities of 1522, 1063, 980, and 944  $\text{mAh g}^{-1}$  are achieved at cycling rates of 0.2, 0.5, 1, and 1.5 C (1 C =  $1675 \text{ mA g}^{-1}$ ), respectively, but also 880  $\text{mAh g}^{-1}$

can still be delivered even at current density at 2 C. It outperforms the CNTs-S/Gh-Tb<sup>4+</sup> (1464, 979, 828, 732, and 617  $\text{mAh g}^{-1}$  at 0.2, 0.5, 1, 1.5, and 2 C, respectively), CNTs-S/Gh-Tb<sup>3+</sup> (1214, 848, 761, 665, and 560  $\text{mAh g}^{-1}$  at 0.2, 0.5, 1, 1.5, and 2 C, respectively), CNTs-S/Gh (1176, 795, 693, 607, and 507  $\text{mAh g}^{-1}$  at 0.2, 0.5, 1, 1.5, and 2 C, respectively) cells, and most previously reported Li-S

batteries (Figure 5F; Table S1). More importantly, as the rate is switched back to 0.2 C (Figure 5E), the CNTs-S/Gh-Tb<sup>3+/4+</sup> cell could recover a reversible capacity of 1042 mAh g<sup>-1</sup> as compared with other cells (981, 856, and 767 mAh g<sup>-1</sup> for CNTs-S/Gh-Tb<sup>4+</sup>, CNTs-S/Gh-Tb<sup>3+</sup>, and CNTs-S/Gh cells, respectively), indicating a good structural stability of the CNTs-S/Gh-Tb<sup>3+/4+</sup> electrode at various rates.

An excellent long-term cyclability could be achieved for the CNTs-S/Gh-Tb<sup>3+/4+</sup> cell as well, as displayed in Figure 5G. The higher reduction of sulfur for the CNTs-S/Gh-Tb<sup>3+/4+</sup> electrode is evident even from the initial discharge capacity of more than 1157 mAh g<sup>-1</sup> at 1 C, whereas 906, 818, and 596 mAh g<sup>-1</sup> is accessible for CNTs-S/Gh-Tb<sup>4+</sup>, CNTs-S/Gh-Tb<sup>3+</sup>, and CNTs-S/Gh electrodes, respectively, suggesting the sulfur utilization is about 70% for CNTs-S/Gh-Tb<sup>3+/4+</sup> against 54%, 48%, and 36% for CNTs-S/Gh-Tb<sup>4+</sup>, CNTs-S/Gh-Tb<sup>3+</sup>, and CNTs-S/Gh electrodes, respectively. As the cycles progress, the CNTs-S/Gh-Tb<sup>4+</sup>, CNTs-S/Gh-Tb<sup>3+</sup>, and CNTs-S/Gh cells probably experience the shuttle effect of losing active sulfur particles, thereby leading to a fast capacity fading (their capacity retentions are 45%, 46%, and 23%, and the capacity fade rates are 0.12%, 0.11%, and 0.15% per cycle, respectively) at the end of the 500th cycle. However, the CNTs-S/Gh-Tb<sup>3+/4+</sup> cell can stably sustain the capacity of above 656 mAh g<sup>-1</sup>, accounting for 56% of the initial capacity, with a capacity decay rate of 0.087% per cycle under the same testing conditions. Consistently with the significant improvement in cycling stability, its average Coulombic efficiency is above 99% during the whole cycling process, illustrating the successful trapping of soluble LiPSs and high sulfur utilization. Besides, the long-term cycling test of CNTs-S/Gh-Tb<sup>3+/4+</sup> at 0.5 C (Figure S39) delivers an initial discharge capacity of ~1115 mAh g<sup>-1</sup> and maintained ~990 mAh g<sup>-1</sup> after 108 successive cycles with stable capacity retention of 89%.

Since a high sulfur mass loading is a key factor to scale up the practical application of the Li-S battery, herein, we further increased the areal sulfur mass loading to 4.1 mg cm<sup>-2</sup>. As shown in Figure 5H, the high-sulfur-loading cells with CNTs-S/Gh-Tb<sup>3+/4+</sup> cathodes exhibit excellent capacity retention with a specific capacity of 993 and 765 mAh g<sup>-1</sup> at the first and the 120th cycle for the 0.1 C cycling test, whereas the cells with CNTs-S/Gh-Tb<sup>4+</sup>, CNTs-S/Gh-Tb<sup>3+</sup>, or CNTs-S/Gh cathodes fail to cycle stably and demonstrate significantly decayed capacities. This comparison further demonstrates the importance of Tb<sup>3+/4+</sup> electron reservoirs in thick sulfur electrodes to accelerate both discharging and charging processes. To further assess the potential of employing Gh-Tb<sup>3+/4+</sup> catalysts under harsh conditions toward a more practical cell, thick sulfur cathodes (areal mass loading of 5.2 mg cm<sup>-2</sup>) with a low E/S ratio of

7.5 μL mg<sup>-1</sup> in coin cells were evaluated. At a relatively large current density of 0.05 C (Figure 5I), Gh-Tb<sup>3+/4+</sup> catalysts still enable the lean-electrolyte Li-S cells with a high initial discharge capacity of 1225 mAh g<sup>-1</sup> along with a capacity decay rate of 0.18% per cycle during 134 cycles.

### 3 | CONCLUSION

In conclusion, we propose a strategy to regulate *f* orbital of Tb electronic reservoir to achieve a smooth and consecutive SRR. By decoupling the different requirements at each step of SRR, we rationally designed mixed-valence Tb (Tb<sup>3+/4+</sup>) with moderate *f* orbital as electron source and drain to reduce activation energy barrier, expedite the interfacial electron/Li<sup>+</sup> transport kinetics and boost both LCR and SCR during charge/discharge processes with passing through an important intermediate S<sub>5</sub><sup>2-</sup>. By virtue of the unique electronic structure of Tb<sup>3+/4+</sup>, the CNTs-S/Gh-Tb<sup>3+/4+</sup> cell delivers a high discharge capacity of 1522 mAh g<sup>-1</sup> at 0.2 C, and displays impressive cycling life with a capacity decay rate of 0.087% after 500 cycles at 1 C under the low sulfur loading. Besides, a high sulfur loading of 5.2 mg cm<sup>-2</sup> and a low E/S ratio of 7.5 μL mg<sup>-1</sup> are also simultaneously attainable, demonstrating the potential of the *f* orbital engineering for the development of high-energy battery systems.

### 4 | EXPERIMENTAL SECTION

Experimental details are provided in the Supporting Information.

#### ACKNOWLEDGMENTS

This research was funded in part by National Natural Science Foundation of China (Grant Nos. 22109119, 51972238 and U21A2081), Natural Science Foundation of Zhejiang Province (Grant Nos. LQ19B030006 and LQ22B030003), Major Scientific and Technological Innovation Project of Wenzhou City (Grant No. ZG2021013), Postgraduate Innovation Foundation of Wenzhou University (Grant No. 316202102051).

#### CONFLICT OF INTEREST

The authors declare no conflict of interest.

#### ORCID

Shuo Yang  <https://orcid.org/0000-0001-8906-5289>

Dong Cai  <https://orcid.org/0000-0002-8775-3480>

Zhi Yang  <https://orcid.org/0000-0002-9265-5041>

## REFERENCES

1. Bruce PG, Freunberger SA, Hardwick LJ, Tarascon JM. Li-O<sub>2</sub> and Li-S batteries with high energy storage. *Nat Mater*. 2011; 11(1):19-29.
2. Lin Z, Liu Z, Fu W, Dudney NJ, Liang C. Lithium polysulfido-phosphates: a family of lithium-conducting sulfur-rich compounds for lithium-sulfur batteries. *Angew Chem Int Ed*. 2013; 52(29):7460-7463.
3. Manthiram A, Chung SH, Zu C. Lithium-sulfur batteries: progress and prospects. *Adv Mater*. 2015;27(12):1980-2006.
4. Pang Q, Liang X, Kwok CY, Nazar LF. Advances in lithium-sulfur batteries based on multifunctional cathodes and electrolytes. *Nat Energy*. 2016;1(1):16132.
5. Zhang X, Chen K, Sun Z, et al. Structure-related electrochemical performance of organosulfur compounds for lithium-sulfur batteries. *Energ Environ Sci*. 2020;13(4): 1076-1095.
6. Zhou S, Yang S, Ding X, et al. Dual-regulation strategy to improve anchoring and conversion of polysulfides in lithium-sulfur batteries. *ACS Nano*. 2020;14(6):7538-7551.
7. Jana M, Xu R, Cheng X-B, et al. Rational design of two-dimensional nanomaterials for lithium-sulfur batteries. *Energ Environ Sci*. 2020;13(4):1049-1075.
8. Yeon JS, Ko YH, Park TH, Park H, Kim J, Park HS. Multidimensional hybrid architecture encapsulating cobalt oxide nanoparticles into carbon nanotube branched nitrogen-doped reduced graphene oxide networks for lithium-sulfur batteries. *Energ Environ Mater*. 2021;5(2):555-564.
9. Zhang L, Liu D, Muhammad Z, et al. Single nickel atoms on nitrogen-doped graphene enabling enhanced kinetics of lithium-sulfur batteries. *Adv Mater*. 2019;31:1903955.
10. Wang D-W, Zeng Q, Zhou G, et al. Carbon-sulfur composites for Li-S batteries: status and prospects. *J Mater Chem A*. 2013; 1(33):9382-9394.
11. Pope MA, Aksay IA. Structural design of cathodes for Li-S batteries. *Adv Energy Mater*. 2015;5:150012.
12. Li C, Xi Z, Guo D, Chen X, Yin L. Chemical immobilization effect on lithium polysulfides for lithium-sulfur batteries. *Small*. 2018;14(4):1701986.
13. Ji X, Lee KT, Nazar LF. A highly ordered nanostructured carbon-sulphur cathode for lithium-sulphur batteries. *Nat Mater*. 2009;8(6):500-506.
14. Li Y, Wang W, Zhang B, et al. Manipulating redox kinetics of sulfur species using Mott-Schottky electrocatalysts for advanced lithium-sulfur batteries. *Nano Lett*. 2021;21(15):6656-6663.
15. Wang D, Luo D, Zhang Y, et al. Deciphering interpenetrated interface of transition metal oxides/phosphates from atomic level for reliable Li/S electrocatalytic behavior. *Nano Energy*. 2021;81:105602.
16. Zhang Y, Deng J, Zhang H, Liu Y, Dai H. Three-dimensionally ordered macroporous Pr<sub>6</sub>O<sub>11</sub> and Tb<sub>4</sub>O<sub>7</sub> with mesoporous walls: preparation, characterization, and catalytic activity for CO oxidation. *Catal Today*. 2015;245(1):28-36.
17. Lim AMH, Zeng HC. Antisolvent route to ultrathin hollow spheres of cerium oxide for enhanced CO oxidation. *ACS Appl Mater Interfaces*. 2021;13(17):20501-20510.
18. Gong Z, Wang J, Zhang K, Li B, Wu W. Complex rare-earth oxides leached from the rare-earth concentrate to prepare the catalyst for selective catalytic reduction of NO with NH<sub>3</sub>. *Miner Eng*. 2020;146:106135.
19. Wang J, Yan Z, Liu L, Zhang Y, Zhang Z, Wang X. Low-temperature SCR of NO with NH<sub>3</sub> over activated semi-coke composite-supported rare earth oxides. *Appl Surf Sci*. 2014; 309(1):1-10.
20. Escudero-Escribano M, Malacrida P, Hansen MH, et al. Tuning the activity of Pt alloy electrocatalysts by means of the lanthanide contraction. *Science*. 2016;352(6281):73-76.
21. Li D, Sun L, Zhu J, Hu L, Guo D. Enhanced oxygen reduction reaction performance of ReO<sub>x</sub>/NC (re = La, Ce, Pr, Sm, Eu, Tb, Er, Tm and Yb)-especially Pr<sub>6</sub>O<sub>11</sub>/NC via accommodating oxygen vacancies and its application for Zn-air battery. *Appl Surf Sci*. 2021;535:147689.
22. Gao H, Zhou Y, Chen K, Li X. Synthesis of Tb<sub>4</sub>O<sub>7</sub> complexed with reduced graphene oxide for Rhodamine-B absorption. *Mater Res Bull*. 2016;77(1):111-114.
23. Morrison G, Spagnuolo NR, Karakalos SG, Zur Loye H-C. Cs<sub>3</sub>RE<sup>III</sup>Ge<sub>3</sub>O<sub>9</sub> (RE = Pr, Nd, and Sm-Yb) and Cs<sub>8</sub>Tb<sup>III</sup><sub>2</sub>Tb<sup>IV</sup>Ge<sub>9</sub>O<sub>27</sub>: a rare example of a mixed-valent Tb(III)/Tb(IV) oxide. *Inorg Chem*. 2019;58(13):8702-8709.
24. Palumbo CT, Zivkovic I, Scopelliti R, Mazzanti M. Molecular complex of Tb in the +4 oxidation state. *J Am Chem Soc*. 2019; 141(25):9827-9831.
25. Han Z, Zhao S, Xiao J, et al. Engineering d-p orbital hybridization in single-atom metal-embedded three-dimensional electrodes for Li-S batteries. *Adv Mater*. 2021;33(44): 2105947.
26. Hulva J, Meier M, Bliem R, et al. Unraveling CO adsorption on model single-atom catalysts. *Science*. 2021;371(6527):375-379.
27. Liu F, Sun G, Wu HB, et al. Dual redox mediators accelerate the electrochemical kinetics of lithium-sulfur batteries. *Nat Commun*. 2020;11(1):5215.
28. Wang R, Luo C, Wang T, et al. Bidirectional catalysts for liquid-solid redox conversion in lithium-sulfur batteries. *Adv Mater*. 2020;32(32):2000315.
29. Chen Q, Chen W, Li Z, Miao B. Mixed valence effects in TbVO<sub>4</sub>:Y nanocrystals and diamagnetic materials: structure, optical linear & nonlinear, magnetic and faraday rotation properties. *J Alloys Compd*. 2021;867:159065.
30. Jia T, Wang W, Long F, Fu Z, Wang H, Zhang Q. Synthesis, characterization and luminescence properties of Y-doped and Tb-doped ZnO nanocrystals. *Mater Sci Eng B*. 2009;162(3): 179-184.
31. Ma Z, Zhou J, Chen Z, Xie E. Luminescence properties of terbium-doped SiCN thin films by rf magnetron reactive sputtering. *Diamond Relat Mater*. 2011;20(4):475-479.
32. Tian L-L, Li S-B, Zhang M-J, et al. Cascading boost effect on the capacity of nitrogen-doped graphene sheets for Li- and Na-ion batteries. *ACS Appl Mater Interfaces*. 2016;8(40):26722-26729.
33. Liang X, Hart C, Pang Q, Garsuch A, Weiss T, Nazar LF. A highly efficient polysulfide mediator for lithium-sulfur batteries. *Nat Commun*. 2015;6(1):5682.
34. Wang S, Qin J, Zheng L, Guo D, Cao M. A self-sacrificing dual-template strategy to heteroatom-enriched porous carbon nanosheets with high pyridinic-N and pyrrolic-N content for oxygen reduction reaction and sodium storage. *Adv Mater Interfaces*. 2018;5(23):1801149.

35. Zhou X, Tian J, Wu Q, Hu J, Li C. N/O dual-doped hollow carbon microspheres constructed by holey nanosheet shells as large-grain cathode host for high loading Li-S batteries. *Energy Storage Mater.* 2020;24(1):644-654.
36. Zhang Y, Yang S, Zhou S, et al. Oxygen doping in antimony sulfide nanosheets to facilitate catalytic conversion of polysulfides for lithium-sulfur batteries. *Chem Commun.* 2021; 57(26):3255-3258.
37. Nandasiri MI, Camacho-Forero LE, Schwarz AM, et al. In situ chemical imaging of solid-electrolyte interphase layer evolution in Li-S batteries. *Chem Mater.* 2017;29(11):4728-4737.
38. Chen W, Lei T, Qian T, et al. A new hydrophilic binder enabling strongly anchoring polysulfides for high-performance sulfur electrodes in lithium-sulfur battery. *Adv Energy Mater.* 2018;8(12):1702889.
39. Feng Q, Wen S, Deng J, Zhao W. Combined DFT and XPS investigation of enhanced adsorption of sulfide species onto cerussite by surface modification with chloride. *Appl Surf Sci.* 2017;425(1):8-15.
40. Wei H, Rodriguez EF, Best AS, Hollenkamp AF, Chen D, Caruso RA. Chemical bonding and physical trapping of sulfur in mesoporous magnéli Ti<sub>4</sub>O<sub>7</sub> microspheres for high-performance Li-S battery. *Adv Energy Mater.* 2017;7(4):1601616.
41. Zhou S, Yang S, Cai D, et al. Cofactor-assisted artificial enzyme with multiple Li-bond networks for sustainable polysulfide conversion in lithium-sulfur batteries. *Adv Sci.* 2022;9(3): 2104205.
42. Zeng G, Liu Y, Chen D, Zhen C, Han Y, He W. Natural lepidolite enables fast polysulfide redox for high-rate lithium-sulfur batteries. *Adv Energy Mater.* 2021;11(44):2102058.
43. Zhao C-X, Li X-Y, Zhao M, et al. Semi-immobilized molecular electrocatalysts for high-performance lithium-sulfur batteries. *J Am Chem Soc.* 2021;143(47):19865-19872.
44. Zhao M, Li X-Y, Chen X, et al. Promoting the sulfur redox kinetics by mixed organodiselenides in high-energy-density lithium-sulfur batteries. *eScience.* 2021;1(1):44-52.
45. Choi HU, Jin JS, Park J-Y, Lim H-T. Performance improvement of all-solid-state Li-S batteries with optimizing morphology and structure of sulfur composite electrode. *J Alloys Compd.* 2017;723(1):787-794.
46. Han J, Jang H, Thi Bui H, et al. Stable performance of Li-S battery: engineering of Li<sub>2</sub>S smart cathode by reduction of multi-layer graphene-embedded 2D-MoS<sub>2</sub>. *J Alloys Compd.* 2021;862: 158031.
47. Deiss E. Spurious chemical diffusion coefficients of Li<sup>+</sup> in electrode materials evaluated with GITT. *Electrochim Acta.* 2005; 50(14):2927-2932.
48. Li S-F, Gu Z-Y, Guo J-Z, et al. Enhanced electrode kinetics and electrochemical properties of low-cost NaFe<sub>2</sub>PO<sub>4</sub>(SO<sub>4</sub>)<sub>2</sub> via Ca<sup>2+</sup> doping as cathode material for sodium-ion batteries. *J Mater Sci Technol.* 2021;78(1):176-182.
49. Peng L, Wei Z, Wan C, et al. A fundamental look at electrocatalytic sulfur reduction reaction. *Nat Catal.* 2020;3(9): 762-770.
50. Yue X-Y, Zhang J, Bao J, et al. Sputtered MoN nanolayer as a multifunctional polysulfide catalyst for high-performance lithium-sulfur batteries. *eScience.* 2022;2(3):329-338.

## SUPPORTING INFORMATION

Additional supporting information can be found online in the Supporting Information section at the end of this article.

**How to cite this article:** Yu S, Yang S, Cai D, et al. Regulating *f* orbital of Tb electronic reservoir to activate stepwise and dual-directional sulfur conversion reaction. *InfoMat.* 2022;e12381. doi:10.1002/inf2.12381